The University of Bradford Institutional Repository

A study of the Quadratic Molecular Stress Function constitutive model in simulation

P. Olley

School of Engineering, Design and Technology/ IRC in Polymer Engineering
University of Bradford
UK

abstract

Constitutive models that conform to separable KBKZ specification have been shown to fit steady-state strain hardening rheological data in planar and uniaxial elongational flows, but with inaccuracy in the rate of strain hardening. The single parameter Molecular Stress Function model of Wagner [Rheol. Acta, 39 (2000), 97-109] has been shown to accurately fit the rise-rate in experimental data for a number of strain hardening and strain softening materials. We study this models accuracy against the well characterised IUPAC LDPE data, and present a method for full implementation of this model for flow solution which is suitable for incorporating into existing separable KBKZ software. A new method for particle tracking in arbitrarily aligned meshes, which is efficient and robust, is given.

The Quadratic Molecular Stress Function (QMSF) model is compared to existing separable KBKZ based models, including one which is capable of giving planar strain hardening; the QMSF is shown to fit experimental rheological and contraction flow data more convincingly. The issue of 'negative correction pressures' notable in some Doi-Edwards based models is addressed. The cause is identified, and leads to a logical method of calculation which does not give these anomalous results.

Keywords: Molecular Stress Function, MSF, simulation, strain hardening, KBKZ, negative correction pressure

1. Introduction

Forms of the separable KBKZ model [1] have had success (though generally within some limit) in modelling a large number of experimental rheological data. Papanastasiou's damping function [2] has been very successful in fitting data for steady-state *uniaxial* elongational viscosity, shear viscosity, and First Normal Stress Difference for both strain hardening and strain softening materials. This has led to considerable success in simulating axisymmetric flows of strain hardening polymer melt [3-9]. The model has also been successful in simulating planar flows of strain-softening melt [6,10-12], but has not been so successful in modelling strain-hardening planar flows as it does not give simultaneous planar strain-hardening and shear softening behaviour [9]. An adaptation of the KBKZ [13] permitted steady state values for planar elongation viscosity, uniaxial elongational viscosity, and shear viscosity to be fitted simultaneously; the rate of strain hardening was, however, below that seen in experimental results [13]. The model has been applied to several flows, including planar flows of strain hardening polymer melt, with improved success due to capturing significant features of strain hardening behaviour [13-15].

Significant improvement, particularly in capturing the rate of strain hardening, is suggested by use of the Molecular Stress Function (MSF) model [16-20]. The MSF

model is based upon considerations of the geometry and stored energy of the polymer segments undergoing deformation; a particular version, the Quadratic Molecular Stress Function (QMSF) model [19] has been shown to fit transient planar elongation, uniaxial elongation, biaxial elongation and First and Second Normal Stress Difference measurements for strain hardening flows. The accuracy of fit is remarkable particularly as only a single adjustable parameter is used in the model. Convective Constraint Release (CCR) [21] is incorporated into the model described in reference [20], in a manner that effectively separates elongational and rotational damping functions. The versions preceding the CCR model can be recognized as following the 'separabilty' assumption [20].

There have been many recent developments in simulation of time-integral viscoelastic flows. Two dimensional time dependent flows have been solved by convecting deformation fields, to achieve a purely Eulerian method [22] ; three dimensional time dependant flows have be modelled using a Lagrangian mesh approach with remeshing, and information transfer, when the mesh becomes distorted [23]. A modified version of the QMSF with CCR has been implemented and applied to membrane inflation [24]. Direct comparison has been made between a time integral model, its differential approximation and an inelastic model in a complex flow [25].

There have been other recent developments in rheological modelling, with a strong emphasis on molecularly based models. Notable amongst these developments are the Pom Pom model [26, 27], and developments in differential models [28,29]. Molecular considerations have led to some models that employ fractional powers of the Finger Strain Tensor [30,31].

The single parameter QMSF model without constraint release, described in reference [19] has been shown to have many strong points. The model also has an elegant physical derivation in its favour, and provides a natural bridge between earlier KBKZ models, and the MSF with CCR model, described in ref. [20]. It is this single parameter QMSF model that this work focuses on.

2. The Molecular Stress Function Model

The Molecular Stress Function (MSF) model is based on the extra-stress, $\tau(t)$ being given by:

$$\tau(t) = \int_{-\infty}^{t} m(t - t') \, \mathbf{S}_{\mathbf{MSF}}(t') \, dt' \, , \qquad \text{Eq.1}$$

where $\mathbf{S}_{\mathbf{MSF}}$ is the strain measure, and $m(t - t')$ is the memory function between time t' in the past, and the current time t. The strain measure of the Molecular Stress Function is given by:

$$\mathbf{S}_{\mathbf{MSF}} = 5f^2 \left\langle \frac{\mathbf{u}' \mathbf{u}'}{u'^2} \right\rangle, \qquad \text{Eq.2}$$

where $\mathbf{u}'$ is a deformed vector given by

$$\mathbf{u}' = \mathbf{F}(t,t')^{-1} \, \mathbf{u}_0 \qquad \text{Eq.3}$$

$\mathbf{F}$ is the deformation gradient tensor between time t' in the past, and the current time t, and $\mathbf{u_0}$ is a vector of (initially) unit length. The brackets : $\langle \; \rangle$, denote the average over the surface of a sphere of unit radius, i.e.:

$$\langle h \rangle = \frac{1}{4\pi}\int_{\Omega} h\, d\Omega .$$

<div align="right">Eq.4</div>

The strain measure, $\mathbf{S_{MSF}}$ is related to the Doi-Edwards Strain Function, $\mathbf{S_{DE}}$, the relationship is:

$$\mathbf{S_{MSF}} = f^2 \mathbf{S_{DE}}$$

<div align="right">Eq.5</div>

Figure 1 suggests the deformations of tube segments, according to the Doi-Edwards model, in an extensional flow. The division by u'^2 in Eq .2 , inherent to the Doi-Edwards strain tensor, normalises the length of the deformed segments, but effectively draws the 'strain ellipse' back to being a 'strain sphere' (see Figure 1). Thus the Doi-Edwards model assumes a constant cross-section under elongation; the orientation of the segments is accounted for, but the stretching of the tube is not accounted for [19]. This indicates the need for 'f^2' in Eq.2.

The value f represents the ratio of initial to final tube diameters a_o/a . The ratio f has been defined as a function of $\langle u' \rangle$, or $\langle \ln u' \rangle$. A pair of parameter-free models are derived from first principles: the Linear Molecular Stress Function (LMSF) is for modelling linear molecules; the parameter-free model is derived as:

$$f^2 = e^{<\ln u'>},$$

<div align="right">Eq.6</div>

in ref. [18],and the Quadratic Strain Function (QMSF) for modelling long chain branched molecules; is derived in ref. [19] in parameter-free form:

$$f^2 = \frac{1}{2}e^{2<\ln u'>} + \frac{1}{2}$$

<div align="right">Eq.7</div>

We concentrate on a recent single-parameter model for f [19] which includes the notion of a maximum tube stretch. This includes the idea of tube-slip at high deformations, which gives rise to a maximum tube stretch; the tube-slip coefficient is defined in terms of stored energy E, and a maximum value of stored energy, E_{max}. The stored energy is proportional to f^2-1. These principles are used to derive single parameter models for the LMSF and QMSF:

For the LMSF:

$$f^2 = 1 + \left(f_{max}^2 - 1\right)\left[1 + \exp\left(-\frac{e^{\langle \ln u' \rangle} - 1}{\left(f_{max}^2 - 1\right)}\right)\right],$$

<div align="right">Eq.8</div>

and for the QMSF:

$$f^2 = 1 + \left(f_{max}^2 - 1\right)\left[1 + \exp\left(-\frac{e^{2\langle \ln u' \rangle} - 1}{2\left(f_{max}^2 - 1\right)}\right)\right].$$

<div align="right">Eq.9</div>

In the remainder of this work, we use LMSF to refer to Eq.8, and QMSF to refer to Eq.9.

The effective difference between the two models is the different rate at which the functions rise to differentiate between linear tube behaviour, and branched (quadratic) tube behaviour. The parameter, f_{max}^2 sets the maximum value that f^2 can attain.

Figure 2 plots $\langle \ln u' \rangle$ against strain for shear, uniaxial elongation and planar elongation. In elongation the value of $\langle \ln u' \rangle$ rises much faster than in shear. Consideration of the Finger Strain Tensor and Eq.3 in shear and elongational flows, indicates that, at high strains, $\langle \ln u' \rangle$ will be approximately equal to strain in elongational flows, whereas it will be of the order of ln(strain) in shear flows. The curves for planar and uniaxial elongation are very close. Figure 3 shows the variation of f^2 with $\langle \ln u' \rangle$ for LMSF and QMSF models. The parameter f_{max}^2 is set equal to 80.0 (as used in later simulations) for the curves shown. The curves both rise to the set maximum; the QMSF reaches the plateau value at a value of $\langle \ln u' \rangle$ of ≈ 3.5, whereas the LMSF reaches the plateau at much higher strains ($\langle \ln u' \rangle \approx 6$).

The model is attractive for a number of reasons: it has a solid physical basis, and has been shown to gives good fits to experimental data for strain hardening and strain softening polymer melts using only a single parameter. It is reasonably easy to implement in code that can solve flows of separable KBKZ fluids, since the same 'backwards tracking' approach can be employed. A good approximation to the Doi-Edwards tensor $\mathbf{S_{DE}}$ can be estimated from the Cauchy and Finger strain tensors using Currie's closure [32]; and a good approximation to $\langle \ln u' \rangle$ can be deduced from the mathematical derivation in the same work. We compute both $\mathbf{S_{DE}}$ and $\langle \ln u' \rangle$ by a direct integration scheme which is applicable to models with and without an analytical evaluation of the spherical integral.

2.1 Computation of an integral over the surface of a unit sphere

The following procedure is used to compute $\langle \ln u' \rangle$ and $\left\langle \dfrac{\mathbf{u}'\mathbf{u}'}{u'^2} \right\rangle$, thus allowing the strain measure, $\mathbf{S_{MSF}}$ to be calculated.

The notation $\langle h \rangle$ implies averaging the function h over the surface of a unit sphere, ie.

$$\langle h \rangle = \frac{1}{4\pi} \int_\Omega h \; d\Omega \qquad\qquad \text{Eq.10}$$

An integration method using points that are (exactly) evenly distributed over a unit sphere was shown to be efficient in ref [33]; the method for setting the positions of the evenly spaced points was not given. We take the approach of calculating integration weights for a grid of elements on the surface of the sphere.

Consideration of Fig. 4 shows that an element of surface at position (θ, ϕ), on a unit sphere, has an area, $d\Omega$, given by:

$$d\Omega = \sin\theta \; d\phi \; d\theta \qquad\qquad \text{Eq.11}$$

where $d\phi$ and $d\theta$ are infinitesimally small increments in ϕ and θ respectively. For numerical integration with finite increments in ϕ and θ, $\Delta\phi$ and $\Delta\theta$ it is appropriate to use:

$$\Delta\Omega = \frac{1}{2}\left(\sin\left(\theta + \frac{\Delta\theta}{2}\right) + \sin\left(\theta - \frac{\Delta\theta}{2}\right)\right)\Delta\theta \ \Delta\phi \ , \qquad \text{Eq.12}$$

which recognises the difference in lengths of opposite edges (in the θ direction) of an element of finite dimensions.

Eq.12 provides weightings for the direct integration scheme used to calculate both $\langle \ln u' \rangle$ and $\mathbf{S_{DE}}$; n_1 elements are used to span the π radians range of θ, and n_2 elements are used to span the 2π radians range of ϕ.

$$\frac{1}{4\pi}\int_{\Omega} h \ d\Omega \approx \sum_{i=1,n_1} \sum_{j=1,n_2} w_{i,j} \ h_{i,j} \qquad \text{Eq.13}$$

$$\text{where:} \ w_{i,j} = \frac{1}{2\widetilde{\Omega}}\left[\sin\left(\theta_i + \frac{\Delta\theta}{2}\right) + \sin\left(\theta_i - \frac{\Delta\theta}{2}\right)\right]\Delta\theta \Delta\phi, \qquad \text{Eq.14}$$

$\Delta\theta = \dfrac{\pi}{n_1}$, $\Delta\phi = \dfrac{2\pi}{n_2}$ and θ_i is computed such that all θ_i are placed in the centre of elements; the first is placed in the centre of an element ranging from $\theta = 0$ to $\theta = \Delta\theta$:

$$\theta_1 = \frac{\Delta\theta}{2} , \qquad \text{Eq.15}$$

then the remaining $n_1 - 1$ positions follow from :

$$\theta_i = \theta_{i-1} + \Delta\theta \ \ \left(\text{for } i = 2,...n_1\right). \qquad \text{Eq.16}$$

Similarly ϕ_j can be computed from

$$\phi_1 = \frac{\Delta\phi}{2} , \qquad \text{Eq.17}$$

then $\qquad\qquad \phi_j = \phi_{j-1} + \Delta\phi \ \ \left(\text{for } \ j = 2,...n_2\right). \qquad \text{Eq.18}$

We use $\widetilde{\Omega}$, in place of 4π, where $\widetilde{\Omega} \ \left(\cong 4\pi\right)$ is the surface area of the sphere as computed by the corresponding non-normalised integration scheme:

$$\widetilde{\Omega} = \sum_{i=1,n1} \sum_{j=1,n2} \left(\frac{1}{2}\left[\sin\left(\theta_i + \frac{\Delta\theta}{2}\right) + \sin\left(\theta_i - \frac{\Delta\theta}{2}\right)\right]\Delta\theta \Delta\phi\right). \qquad \text{Eq.19}$$

This computation needs performing only once for the chosen n_1 and n_2 and has the effect of reducing systematic error due to finite integration.

For clarity, the value of $h_{i,j}$ in Eq.13 is the value of h at position $\left(\theta_i, \phi_j\right)$.

In the particular case of calculating $\mathbf{S}_{DE}$ and $\langle \ln u' \rangle$, it is necessary to specify the deformed vector $\mathbf{u'}$ corresponding to a polar position (θ, ϕ); this is calculated from $\mathbf{u'} = \mathbf{F(t,t')}^{-1} \mathbf{u}_0$, where

$$\mathbf{u}_0 = \begin{vmatrix} u_x \\ u_y \\ u_z \end{vmatrix} = \begin{vmatrix} \sin\theta \, \cos\phi \\ \sin\theta \, \sin\phi \\ \cos\theta \end{vmatrix}. \qquad \text{Eq.20}$$

Thus at each angular position, $\ln u'$ is calculated using:

$$\ln u' = \ln\left(\sqrt{{u'_x}^2 + {u'_y}^2 + {u'_z}^2} \right) = \frac{1}{2}\ln\left({u'_x}^2 + {u'_y}^2 + {u'_z}^2 \right), \qquad \text{Eq.21}$$

and $\dfrac{\mathbf{u'u'}}{u'^2}$ can be computed at that polar position.

Note that for $\mathbf{F} = \mathbf{I}$, the computation of $\mathbf{S_{DE}} = 5\left\langle \dfrac{\mathbf{u'u'}}{(u')^2} \right\rangle$ should give exactly

$\mathbf{S_{DE}}\big|_{\mathbf{F=I}} = \dfrac{5}{3}\mathbf{I}$. Due to the errors inherent in finite integration, the computed value will differ from this, introducing a small artificial difference into the diagonal terms in the strain tensor, this gives a small, artificial, normal stress difference. This small artifact is, however, sufficient to give large errors in calculations of apparent viscosity at low strains. Hence, denoting the directly computed value of $\mathbf{S_{DE}}$ at $\mathbf{F=I}$ by $\widetilde{\mathbf{S}}_{\mathbf{DE}}\big|_{\mathbf{F=I}}$, and denoting the directly computed value of $\mathbf{S_{DE}}$ at a general value of $\mathbf{F}$ by $\widetilde{\mathbf{S}}_{\mathbf{DE}}$, we reduce the systematic error in the computation of $\mathbf{S_{DE}}$ by using:

$$\mathbf{S_{DE}} = \widetilde{\mathbf{S}}_{\mathbf{DE}} + \frac{5}{3}\mathbf{I} - \widetilde{\mathbf{S}}_{\mathbf{DE}}\big|_{\mathbf{F=I}}. \qquad \text{Eq.22}$$

2.2   Comparison of MSF model with Rheological data

The model has been demonstrated to accurately fit experimental data for strain hardening and strain softening polymers in many different extensional experiments. We assess this model against data for the well-characterised IUPAC LDPE. We assume that the memory term in Eq. 1 can be represented by the well known sum of exponential decay constants:

$$m(t - t') = \sum_i \frac{g_i}{\lambda_i} e^{-(t-t')/\lambda_i}, \qquad \text{Eq.23}$$

where λ_i and g_i are relaxation times and relaxation modulii, respectively. The constitutive data used is Laun's data for IUPAC LDPE at 150°C (from refs.[34,35]) The data is reproduced in Table 1, along with temperature-shifted data at 125°C and 160°C.

Figure 5 compares QMSF model with transient viscosity data for IUPAC LDPE that were made at 125°C. A rate of 0.05s^{-1} was used for shear, uniaxial elongational, and planar elongational measurements. The fit was obtained with $f_{max}{}^2$ set to a value of 80;

the value was chosen to optimise the fit to the transient elongational data. It is immediately apparent that both uniaxial and planar strain-hardening are being exhibited by the model (as shown in ref. [19]). The rise rate of the elongational data is matched closely. This rise rate is largely independent of the actual value of f_{max}^2 that is used in the QMSF model; the value of f_{max}^2 that is chosen effectively sets the plateau value for elongational viscosity, and only affects the rise rate significantly in the region shortly before the plateau. The shear viscosity is slightly higher than the experimental data. It is interesting to compare the results with curves for the LMSF, and also the adapted KBKZ described in ref. [13]. A value of f_{max}^2 of 80 was again used for the LMSF (raising the value above 80 has very little effect on computed viscosity, since f_{max}^2 is reached at very large strains in the LMSF). The adapted KBKZ was used with 2 parameters (α =2.5 and β=0.003) as employed for fitting steady-state IUPAC data in [13]. Figure 6 compares the three models against transient planar elongational data at 0.05s^{-1}. The LMSF model is seen to have lower natural rise-rate than the QMSF. Interestingly the rise-rate of the adapted KBKZ (which was noted to rise too slowly, compared with the strain hardening data [13]) follows a similar path to the LMSF.

Having obtained a value for f_{max}^2 (obtained from fitting transient elongational data only) it is interesting to plot the results thus predicted for steady-state viscosity against the well known steady state data for IUPAC LDPE (from[34 - 36]). The results are plotted in Figure 7. It is noted that shear viscosity and N1 are significantly higher than the experimental data. The data for uniaxial elongational is under predicted at low elongational rates, and over predicted at high elongational rates - a situation that appears to be 'normal' for models that do not use different parameters for different relaxation modes. Whilst we do not believe that it is within the 'spirit' of the model to use different parameters for different relaxation times: "$(f_{max}^2)_i$ " , we can confirm that the adoption of this multi-parameter method does give a very close fit to both transient and steady state elongational data, with a reduced over-prediction of shear and N1 data. By contrast the adapted KBKZ described in [13] does not give a good fit to the transient data when used with a similar number of parameters; earlier versions of the KBKZ did not give strain hardening in planar elongational flow[13]. It should be noted that the single fitting parameter was based upon obtaining the best fit to the transient elongational data (as opposed to a value that was a compromise, in some sense, between all rheological data). Other values for f_{max}^2 gave some improvement to the fitting of shear viscosity, and N1, but at cost to the fitting of transient elongational data.

3.   Simulation method

A finite element based solution method has been implemented to find the flow solution for flows obeying the QMSF model. Overall, the requirements for solving these flows are similar to the requirements for solving other time-integral models, such as the separable KBKZ; the integration of the strain measure tensor, $\mathbf{S_{MSF}}$, detailed earlier in this work, is the largest required addition. Significant improvements are detailed for particle tracking through elements, and for the time-integration of the deformation gradient tensor, over the methods described in ref. [13]; these methods follow on from methods developed by Dupont and Crochet [3], and Luo and Mitsoulis [4].

3.1   Overview of the solution method

The simulation uses 9-noded bi-quadratic elements to represent velocity components, with one order lower interpolation used for pressure. The simulation begins with a Newtonian flow solution. For each Gauss point in each element, the strain history is calculated by tracking the past history of a 'particle' of fluid back upstream. A typical trajectory will be through many elements; it is necessary to determine which element the particle has reached and the velocity and velocity gradient information at that point. This information allows the deformation gradient tensor to be tracked, and from this the strain function $\mathbf{S_{MSF}}$ can be computed. Obtaining the strain function over the particles history permits Eq.1 to be integrated. We use a large number of 5 point Gauss-Legendre elements for this time integration.

3.2   Particle tracking

To compute the stress state at a position according to time-integral equations, the deformation history of a particle must be computed. A particles trajectory is tracked backwards using a standard kinematic procedure:

$$\widetilde{x}(t'-\delta t') = x(t') - u\,\delta t' + \frac{\delta t'^2}{2}\left(u\frac{\partial u}{\partial x} + v\frac{\partial u}{\partial y} \right), \qquad \text{Eq.24}$$

$$\widetilde{y}(t'-\delta t') = y(t') - v\,\delta t' + \frac{\delta t'^2}{2}\left(u\frac{\partial v}{\partial x} + v\frac{\partial v}{\partial y} \right), \qquad \text{Eq.25}$$

where $(\,x(t')\,,\,y(t')\,)$ is the particles position at time t', and $(\,\widetilde{x}(t'-\delta t')\,,\,\widetilde{y}(t'-\delta t')\,)$ is the particles approximate position a small increment in time, $\delta t'$, earlier. As discussed in ref [13], the approximate position will not lie precisely on the original streamline. The position is now adjusted back onto its original streamline with a movement normal to its velocity using:

$$x(t'-\delta t') = \widetilde{x}(t'-\delta t') + \delta x, \qquad \text{Eq.26}$$
$$y(t'-\delta t') = \widetilde{y}(t'-\delta t') + \delta y, \qquad \text{Eq.27}$$

where
$$\delta x = k\frac{\partial \psi}{\partial x}, \qquad \text{Eq.28}$$

$$\delta y = k\frac{\partial \psi}{\partial y}, \qquad \text{Eq.29}$$

and
$$k = \frac{\psi_0 - \widetilde{\psi}}{\left(\frac{\partial \psi}{\partial x} \right)^2 + \left(\frac{\partial \psi}{\partial y} \right)^2} \qquad \text{Eq.30}$$

The streamfunction is ψ, ψ_0 is the value of streamfunction at the Gauss point where tracking began, and $\widetilde{\psi}$ is the value of streamfunction at the approximate position. The method prevents the accumulation of small errors in tracking, giving both improved accuracy and convergence. The derivation is given in [13].

3.2.1 Determining the current element and element co-ordinates

In a finite element based implementation, a principal difficulty lies in determining which element that a position, defined by $(\,x,y\,)$, lies in. Additionally to obtain any information on nodal variable and their derivatives, the position must be mapped to the elements natural co-ordinates $(\,\xi,\eta\,)$. It is possible to use a rectangular grid of

elements, which makes element identification possible through a direct mapping; however this limits flexibility in meshing. The streamline tracking method of Luo and Tanner [38] identified the element that shared the edge through which the previously 'occupied' element was exited; this allowed flexible meshing. The method now described identifies both the element that contains an arbitrary (x, y) position, and the corresponding element coordinates. The method has broad application to other tracking and remeshing problems.

For each element, a polynomial (in x, and y) is obtained for the element natural coordinates. For 2 dimensional natural coordinates ξ and η

$$\xi = f_1(x, y) \quad \text{and} \quad \eta = f_2(x, y) \qquad \text{Eqs.31}$$

The appropriate terms in x and y to use for a given element can be determined from 'Pascals triangle' (or more prosaically by noting the powers of ξ and η that are used in the elements interpolation functions, and using the same powers of x and y). Thus for a nine node bi-quadratic element we have:

$$f(x, y) = a_1 + a_2 x + a_3 y + a_4 xy + a_5 x^2 + a_6 y^2 + a_7 x^2 y + a_8 xy^2 + a_9 x^2 y^2 \quad \text{Eq.32}$$

where the coefficients, a_j are initially unknown. To find the coefficients, for the equation for ξ for example, one can use the known values (x_i , y_i , ξ_i) at each of the 9 nodes, to give an equation:

$$\xi_i = a_1 + a_2 x_i + a_3 y_i + a_4 x_i y_i + a_5 x_i^2 + a_6 y_i^2 + a_7 x_i^2 y_i + a_8 x_i y_i^2 + a_9 x_i^2 y_i^2 \quad \text{Eq.33}$$

Repeating over the 9 nodes of the element gives a system of 9 equations: this can be solved to provide the coefficients of a_j for ξ in that element. Similarly a function for η can be obtained for that element, and this repeated to cover all elements. The process needs performing only once unless the mesh is altered.

An elements natural coordinates have a definite valid range (normally $\xi_{min} \leq \xi \leq \xi_{max}$ and $\eta_{min} \leq \eta \leq \eta_{max}$ for 2D quadrilateral elements). It can be determined if a position (x, y) could be within an element by checking that the natural coordinates given by Eq.31 is within this allowed range (with a small allowance). The position given by the element interpolation functions, (x_e , y_e) is now computed using the usual interpolation.

$$x_e = \sum \phi_j x_j ; \quad y_e = \sum \phi_j y_j \qquad \text{Eq.34}$$

This position will generally be found to be differ from the original position by an amount given by δx and δy where:

$$\begin{vmatrix} \delta x \\ \delta y \end{vmatrix} = \begin{vmatrix} x - x_e \\ y - y_e \end{vmatrix} \qquad \text{Eq.35}$$

A form of Newtons approximation can be used to find the small changes in $\delta \xi$ and $\delta \eta$ that are required to give the original positions:

$$\begin{vmatrix} \delta \xi \\ \delta \eta \end{vmatrix} = \left(\mathbf{J}^T \right)^{-1} \begin{vmatrix} \delta x \\ \delta y \end{vmatrix} \qquad \text{Eq.36}$$

Note that $\mathbf{J^T}$ is the transpose of the Jacobian most commonly used in finite element computation, ie.

$$\mathbf{J} = \begin{vmatrix} \dfrac{\partial x}{\partial \xi} & \dfrac{\partial y}{\partial \xi} \\ \dfrac{\partial x}{\partial \eta} & \dfrac{\partial y}{\partial \eta} \end{vmatrix}$$

Eq.37

One or two iterations will normally obtain values of ξ and η that return the input position to within negligible error.

A complication can arise: due to 'multiple root' behaviour of quadratic and higher based elements, it is possible to find more than one element for which Eq.31 gives 'valid-range' values of ξ and η. These can usually be eliminated immediately if the values of $(\delta x, \delta y)$ from Eq.35 are larger than the largest dimension of the element. More subtle 'aliases' can be identified after an iteration of the Newton's approximation method, which will give values of ξ and η that are outside the valid range.

3.2.2 Tracking Efficiency
The key to making the method efficient is to maintain, for each element, a list of the neighbouring elements that exiting particles have previously been tracked into. For most elements this will contain only 1, 2, or 3 elements. Upon finding that a particle has left a particular element, the elements in this elements 'list of previously tracked into' are checked first; this will normally yield the correct new element without extensive searching of the whole mesh.

The computation of the coefficients for ξ and η over $\sim 10^3$ elements takes only a fraction of a second in total on a modern PC. The method is robust, and appears general for 1D, 2D and 3D Legendre-type elements.

3.3   Time integration of the extra-stress tensor
The time integration of Eq.1 is accomplished by employing five point Gauss-Legendre integration of each of a large number of time segments. At each of these Gauss point the deformation rate tensor, $\mathbf{L}(t')$, is constructed where $L_{ij} = \partial u_i / \partial x_j$.
Continuous velocity gradients are used to construct $\mathbf{L}(t')$ (computed by the least-squares method described in [37]). For the Legendre type of element used, incompressibility is enforced in an average sense; it is to be expected that at any general point, $L_{11} + L_{22} + L_{33} = \varepsilon$, where ε represents the error in incompressibility. This error is 'shared' between the three diagonal components of $\mathbf{L}$ to maintain a physically meaningful deformation gradient tensor; see [9].

The deformation gradient tensor is computed by solution of :

$$\frac{d\,\mathbf{F}(s)}{d\,t} = \mathbf{L}(t')\mathbf{F}(s) \; ,$$

Eq.38

where $s = t - t'$ [37]. We use a 4th order Runge-Kutta method to calculate $\mathbf{F}$. For accuracy we solve Eq.38 by repeatedly applying the Runge-Kutta process over small time increments $\delta(\delta s)$ which may be far smaller than the time-steps indicated by either the requirements for tracking or the requirements for time-integration of Eq. 1. Previously we have ensured that $\delta(\delta s) \times |L_{ij}| \leq 1/50$ for any element of the tensor $\mathbf{L}$ [13]. An analytical solution of Eq.38 indicates that it is the *largest eigenvalue* of $\mathbf{L}$, K_{max}, that sets the growth rate of $\mathbf{F}$ with time; the time step employed in solving Eq.38 should then be related to K_{max}. The largest eigenvalue of $\mathbf{L}$ can be obtained for little computational cost using the 'power method' e.g. [39]. For current simulations we ensure that $\delta(\delta s) \times K_{max} \leq 1/4$ which appears to give similar accuracy and robustness as the previous criteria, but is significantly faster in practise as the approach identifies, accurately, where small time steps are needed to compute $\mathbf{F}$, and where large time steps are permissible.

The Doi-Edwards strain measure, $\mathbf{S_{DE}}$ and $\langle \ln u' \rangle$ can then be calculated, from $\mathbf{F}$, using the integration formulae in section 2.1. This allows $\mathbf{S_{MSF}}$ to be computed using Eqs.5, 8, and 9. Given that the history of $\mathbf{S_{MSF}}$ is known, the extra-stress tensor, τ, can be calculated by time-integration of Eq.1.

3.4 Updating the velocity and pressure fields

Upon computing a new stress field, an updated velocity and pressure field is required. The method used is an adaptation of the method given in ref [40]. The details of our finite element based implementation of the method are given in ref [13]; only an outline is given here.

For an assumed steady-state solution, with negligible inertia and body forces, we require:

$$\nabla \cdot \boldsymbol{\sigma}_{\mathbf{v}} = 0, \qquad\qquad\qquad \text{Eq.39}$$

where $\boldsymbol{\sigma}_{\mathbf{v}}$ is the total viscoelastic stress, ie $\boldsymbol{\sigma}_{\mathbf{v}} = \boldsymbol{\tau}_{\mathbf{v}} - \mathbf{I}\, p$, where $\boldsymbol{\tau}_{\mathbf{v}}$ is the viscoelastic extra-stress, p is pressure, and $\mathbf{I}$ is the identity matrix. The velocity is now introduced by subtracting notional Newtonian extra-stresses from both sides (the Newtonian stresses are given by $\mu(\mathbf{L} + \mathbf{L^T})$ where μ is a viscosity, and $\mathbf{L}$ is the deformation rate tensor). This leads to:

$$-\nabla.\left(\mu\left(\mathbf{L} + \mathbf{L^T}\right) - \mathbf{I}\, p\right)\Big|_{N+1} = \nabla.\left(\tau_v - \mu\left(\mathbf{L} + \mathbf{L^T}\right)\right)\Big|_{N} . \qquad \text{Eq.40}$$

The subscripts imply that viscoelastic stresses and Newtonian stresses from iteration N are used to calculate the N+1 th velocity and pressure field. The full finite element formulation is given in ref [13]. The AVSS scheme [41] uses a similar method but with individual values of μ for each element.

The value of μ that is used is important: we use $\mu = \omega \mu_0$, where μ_0 is the numerically predicted low rate shear viscosity given by $\mu_0 = \sum g_i \lambda_i$ and ω is a relaxation parameter. If ω is chosen too large, then convergence will be attained excessively slowly; if ω is chosen too small then large instabilities will occur. In these simulations on a model that (accurately) predicts the steep strain hardening curve of IUPAC LDPE, ω needed setting to values of between 2 and 50.

Convergence criteria for the simulations was that $\omega \Delta V_r < 10^{-3}$, where ΔV_r is the maximum change in any velocity component, divide by the maximum flow velocity. A relative pressure change of 10^{-2} or better was obtained for all flow solutions.

4 Determination of Correction Pressure in Doi-Edwards based models

Special considerations are found to be necessary for some Doi-Edwards based (and some other) constitutive models when calculating correction pressure from simulation results. It has been suggested that QMSF based models give negative correction pressures, which has been used as a major criticism. The following demonstrates the potential for these apparently negative correction pressures (in Doi-Edwards based, and also in some KBKZ models), and gives a logical approach to resolve this anomaly. The difference between inlet and outlet pressures has often been referred to as 'the die pressure drop' in simulation work, without indication of measuring points. A study of the dependence of calculated values for δP_{en} for different measuring points (centreline to wall) in ref. [7] showed a moderate variation when using the PSM model without any contribution from the Cauchy tensor. We show, with reasons, a much stronger dependence of δP_{en} on measuring point for the QMSF model.

Correction pressure, δP_{en}, is defined as

$$\delta P_{en} = \frac{P_{in} - P_{out} - \Delta P_u - \Delta P_d}{2\tau_w}$$
    Eq.41

where P_{in} is the inlet pressure to the contraction die, P_{out} is the outlet pressure of the contraction die, ΔP_u is the pressure drop expected from fully developed wall shear stress in the upstream section, and ΔP_d is the pressure drop expected from fully developed wall shear stress in the section downstream of the contraction. For a capillary of length, L, wall shear stress, τ_w, and radius, R the expected pressure drop is $2 L\tau_w / R$; similarly for a planar slit of half-height, h, the expected drop is $L\tau_w / h$. Consider a fully developed planar flow in a slit, with the flow in the x-direction. The velocity components in the y and z directions (v and w respectively) are both zero. The flow will have a different shearing rate at different values of 'y'. Consider that Cauchy's equation for motion in the y-direction is:

$$\frac{\partial}{\partial x}\sigma_{xy} + \frac{\partial}{\partial y}\sigma_{yy} = 0$$
    Eq.42

for steady flow. For fully developed flow we have $\frac{\partial}{\partial x}\sigma_{xy} = 0$, hence:

$$\frac{\partial}{\partial y}\sigma_{yy} = \frac{\partial}{\partial y}(\tau_{yy} - p) = 0,$$
    Eq.43

where τ_{yy} is the extra-stress, and p is pressure.
Consider first Newtonian flow: for Newtonian flow, τ_{yy} is proportional to $\frac{\partial v}{\partial y}$

which is equal to zero for this x-direction flow. It follows from Eq.43 that $\frac{\partial p}{\partial y}$ is zero

for a Newtonian flow – this gives the familiar 'vertical' contours of pressure similar to

those shown in Figure 8 (a). Hence the pressure at a point on the centreline will be the same as the pressure at the corresponding point on the wall.

Consider now separable KBKZ type equations; the strain measures are the Finger strain tensor, with (sometimes) a contribution from the Cauchy strain Tensor. In the steady state shearing flow being considered, τ_{yy} comes from the "yy" component of the Finger strain tensor (=1 in shear) and the "yy" component of the Cauchy tensor (= γ^2 +1 in shear).

If only the Finger Strain Tensor is used then $\dfrac{\partial \tau_{yy}}{\partial y} \cong 0$, and thus $\dfrac{\partial p}{\partial y} \cong 0$ (the gradient is not exactly zero, since the stress also depends on the damping and memory functions, which are affected by shear rate). If $\mathbf{C}^{-1} - \mathbf{I}$ is used in place of $\mathbf{C}^{-1}$, then τ_{yy} will be identically zero in the shear flow described and vertical contours of pressure are seen (see Figure 8 (a)). If the model employs a non zero contribution from the Cauchy Tensor, then the "γ^2 +1" term in shear contributes directly to τ_{yy}; as a result $\dfrac{\partial \tau_{yy}}{\partial y} \neq 0$, and according to Eq. 43 there will be a pronounced pressure gradient in the "y" direction. The qualitative implications above are all confirmed in simulation.

We lastly consider the Doi-Edwards strain tensor, or to be precise Currie's approximation to it [32]. This approximates the Doi-Edwards strain tensor as a weighted sum of the Finger strain tensor, and the Cauchy tensor. The same logic that is used for the separable KBKZ model implies that the pressure gradient, normal to the direction of flow, will be non zero, certainly if Currie's approximation is used. Simulation results confirm this for a full implementation of the Doi-Edwards strain measure. The gain give by f^2 in the MSF model has the affect of magnifying this effect (compare (b) and (c) in Figure 8).

Constitutive Model	Pressure gradient normal to fully developed shear flow	comment
Newtonian	Zero	pressure contours normal to flow
KBKZ using Finger strain tensor $\mathbf{C}^{-1}$	$\neq 0$	weak effect, Second Normal Stress Difference, N_2=0
KBKZ using $\mathbf{C}^{-1}$ - $\mathbf{I}$	Zero	N_2=0
KBKZ using Finger and Cauchy strain tensor	$\neq 0$	Strength of effect depends upon relative weighting of Finger and Cauchy tensors
Doi-Edwards Strain tensor	$\neq 0$	Moderate effect, no strain hardening
QMSF	$\neq 0$	Pronounced effect, includes strain hardening

To resolve the problem of "negative correction pressures" with models that give a non-zero '$\partial p/\partial n$', as defined above, it is necessary to measure P_{in}, and P_{out} at the wall – not at the centreline. This seems appropriate since the correction pressures can be viewed as a means of comparing actual pressure drop, with the pressure drop expected solely from shear at the walls. We can confirm that measuring P_{in} and P_{out} at the *centreline* does give strong negative values of "correction pressures", particularly at high flow rates, for the QMSF model (example values are given in section 5.1). For the models for which '$\partial p/\partial n$' is zero, the change makes no difference (provided that a fully developed inlet flow profile is used as a boundary condition). The values of correction pressure that we list are all obtained from measurements at the wall.

5. Evaluation of QMSF model in flow simulation

We report a number of simulations that indicate the behaviour of the QMSF material model in planar and axisymmetric contraction die flows. This behaviour is compared with the 'PSM' KBKZ model [2], which is known to give good agreement with experimental data for opening angle for 4:1 axisymmetric flow of IUPAC LDPE; it is also known that it does not give strain hardening response in planar flows. Additional comparison is made to the 'adapted' KBKZ model [13], which does give strain hardening in both axisymmetric and planar flows, but which underestimates the strain hardening *rate* for branched polymer melts [13].
Measures which are compared include the vortex opening angle (using a definition that is suitable for both 'convex' and 'concave' vortexes, given in ref. [13]), and the vortex intensity (see [3], or [37] for definition). A third measure that is investigated is the correction pressure; this is evaluated for all models as described in section 4. For clarity, the one-parameter QMSF model (Eq.9) is used with $f^2_{max} = 80.0$. All models used the rheological data for 160°C shown in Table 1. The 'adapted' KBKZ and the 'PSM' KBKZ and the adjustable parameters that were used are specified in Table 2.

5.1 Flow in a 8:1 contraction ratio planar die
Figure 9 shows the vortex details obtained using the QMSF model at apparent shear rates of 4, 16, and 64s^{-1}. For comparison the corresponding plots for the adapted KBKZ model are plotted. It is apparent that vortex size increases with flow rate, as found experimentally; the QMSF model gives a larger and stronger vortex.

Vortex area is indicated by the opening angle, as shown in Figure 10. The QMSF gives steadily increasing vortex angle, once expansion begins at around 0.5s^{-1}. Both QMSF and adapted KBKZ are seen to give a larger vortex with increasing flow rate in planar contraction flows, in keeping with experimental observation. Vortex angle is generally greater with the QMSF model. The PSM model, as shown previously [9], is seen to give a vortex angle that decreases with flow rate, in contrast to experimental observation.

 Figure 11 plots the vortex intensities against shear rate for the QMSF, PSM, and adapted KBKZ. The QMSF model gives a much earlier and stronger rise in vortex intensity than the adapted KBKZ. A peak in vortex intensity is seen at around 32 s^{-1} for the QMSF model; although the vortex size and angle continues to rise after this peak.

The correction pressures are shown in Figure 12, in all case these are calculated using the inlet and outlet pressures at the die walls as discussed earlier. Using wall pressures, the QMSF model is seen to give a positive correction pressure at all flow rates. The QMSF model shows a steeper rise in correction pressures at high flow rates, which is consistent with the model showing the most strain hardening at moderate strains. The adapted KBKZ shows considerably lower correction pressures. The PSM model shows the lowest correction pressures, which seems consistent with its lack of strain-hardening in planar flows.

The levels of Correction Pressure for the QMSF model at low flow rates are of interest: in this planar flow they appear to asymptote to zero, and have not been found to go below zero, even at much lower flow rates than those shown. If the inlet and outlet pressures on the centreline are used, then negative correction pressures would obtained (for example the correction pressure at $0.5s^{-1}$ is -0.50, and at $32s^{-1}$, the correction pressure is -2.0). Negative values of 'correction pressure' are highly questionable from a physical point of view; our use of wall pressures appears logical when a parameter is being calculated that relates *wall* shear and associated pressure drop.

5.2 Flow in a 4:1 contraction ratio axisymmetric die
The QMSF model appears to be a significant improvement over the adapted KBKZ and PSM models in planar contraction flow; the models are here compared in a 4:1 abrupt contraction axisymmetric flow to give an indication as to which features are generally true of the models.
Figure 13 compares the opening angles obtained. The PSM model is known to be quite accurate on this measure, and is reported to be around 2° below experimental results [3]. By comparison the QMSF model, and adapted KBKZ fall short, with the QMSF model being closer.
Figure 14 shows the vortex intensities obtained. The PSM model gives the highest intensity, and the adapted KBKZ the weakest. In this flow the QMSF model exhibits a peak in vortex intensity at a lower rate, around 4 s^{-1}; thus the elongation rate at which peak vortex intensity is seen differs by a factor of four between the two flows. The adapted KBKZ also shows a peak in vortex intensity at around 16 s^{-1}.
The correction pressures are shown in Figure 15. In addition to giving largest vortex growth in this flow, the PSM model is seen to give the largest correction pressures. The correction pressures from the QMSF model stay away from zero in this flow. Interestingly, the correction pressures from the adapted KBKZ model are similar to those from the PSM model until a rate of 8 s^{-1}, after this point they are similar to the QMSF model.

Over both geometries the simulation results from the QMSF model are the most convincing: the results are closer to the experimental measurements in axisymmetric flow than the adapted KBKZ, and far better than the PSM in planar contraction flow. The PSM model apparently gives the best results of the three models in the 4:1 axisymmetric flow, but as it gives qualitatively incorrect results with geometry change from axisymmetric contraction to planar contraction, it seems unsafe to assume that it will be reliable for flows with significant non-axisymmetric elongation.

6. Discussion and conclusions

The 'adapted KBKZ' model improved over the 'PSM KBKZ' model in the sense that it allows strain hardening in planar flows to be modelled. The form of Quadratic Molecular Stress Function model that has been implemented and studied has many features that make it more appealing than the 'adapted KBKZ' model. It has a more solid physical derivation, and only one adjustable parameter. Within the confines of one parameter the model gives a good fit to transient and steady-state elongational viscosities for IUPAC LDPE, and has previously been shown to give very good agreement with other viscometric measures for strain-hardening polymers [19]. Capturing the rate of strain-hardening is a particularly important improvement over the adapted KBKZ model. In simulations of converging flow in an axisymmetric die the model gives vortex sizes that are nearly as close to experiment as those given by the PSM model, and are significantly closer than those given by the adapted KBKZ. In planar contraction flows, where the PSM model fails to predict even a qualitative vortex growth (due to lack of planar strain hardening), the QMSF model gives strong and early vortex growth; again it appears to improve significantly over the adapted KBKZ. This particular form of the QMSF model (with one adjustable parameter) gives some degree of over-prediction of steady state shear viscosity and First Normal Stress Difference for IUPAC LDPE, when the single parameter is obtained from transient elongational viscosity.

A different model, the Linear Molecular Stress Function (LMSF) model must be employed if modelling a linear polymer that exhibits strain softening.

Implementation of the model is not particularly difficult compared with a KBKZ implementation; in particular the model is readily implemented in a 'backwards time-integration' method as normally used for the KBKZ model. It is possible to compute the Doi-Edwards tensor and <ln u′> by direct integration, a method that has application to models with or without an analytical evaluation or approximation of the spherical integral.

The particle/element tracking methods described have proven valuable in making this 'tricky' part of stress calculation robust, and self-contained. In particular, the method is general for different element of the Legendre class, provided that the same order of interpolation is used in all principal directions. The method works efficiently on meshes where the elements change alignment with respect to coordinate axes, or flow. The simple technique of recording the most common element changes, and checking these first, keeps search-time close to a minimum. The method has broad application to other tracking and remeshing problems.

There is some cost involved: direct integration of $\mathbf{S_{DE}}$ and <ln u′> is computationally expensive, with simulation times increased by a factor of around three using our integration method. An approximation to <ln u′> can be deduced from the derivation of the approximation for $\mathbf{S_{DE}}$ in ref. [32][1]. We consider this approximation to be 'very good' in elongation, and 'good' in shear (e.g. 5% and 15% over-estimate of <ln u′> at

---

[1] Thanks to a referee for pointing this out, we take the approximation to be

$$\langle \ln u' \rangle \approx 0.5 \ln \left(\frac{1}{7} \left(I_1 + 2 \left(I_2 + \frac{13}{4} \right)^{0.5} - 1 \right) \right)$$

16

shear values of 10 and 100 respectively). This approximation would remove the increase in computation time if found satisfactory for simulation.

Convergence was generally more difficult to achieve than with the adapted KBKZ model, we believe this is due to the high strain-hardening rates that can be accurately fitted. Significantly higher relaxation was needed, with a corresponding increase in the number of iterations that were required for convergence. This difficulty does not appear to be a problem with the QMSF model, but a difficulty of simulating flows with strong strain hardening, when this strain hardening is accurately captured in the constitutive model.

References

[1] Wagner M.H., A constitutive analysis of uniaxial elongational flow data of low-density polyethylene melt , J.Non-Newt.Fluid Mech., 4 (1978), 39.

[2] A.C. Papanastasiou, L.E. Scriven and C.W. Macosko., An Integral Constitutive Equation for Mixed Flows: Viscoelastic Characterization ,J. Rheol., 27 (1983), 387.

[3] S. Dupont and M.J. Crochet, The vortex growth of a K.B.K.Z. fluid in an abrupt contraction , J.Non-Newt.Fluid Mech., 29 (1988), 81.

[4] X.-L Luo and E. Mitsoulis, A numerical study of the effect of elongational viscosity on vortex growth in contraction flows of polyethylene melts , J. Rheol., 34 (1990), 309.

[5] A. Goublomme. Ph.D. Thesis, Louvain-la-Neuve, (1992)

[6] D.G. Kiriakidis, H.J. Park, E. Mitsoulis, B. Vergnes and J.-F. Agassant., A study of stress distribution in contraction flows of an LLDPE melt , J.Non-Newt.Fluid Mech., 47 (1993), 339.

[7] B. Bernstein, K. A. Feigl, E. T. Olsen, Steady flows of viscoelastic fluids in axisymmetric abrupt contraction geometry: A comparison of numerical results J. Rheol. 38 (1994), 53.

[8] R. Ahmed, R.F. Liang and M.R. Mackley, The experimental observation and numerical prediction of planar entry flow and die swell for molten polyethylenes , J. Non-Newt. Fluid Mech., 59 (1995), 129.

[9] Olley, P.,Spares, R., and Coates, P.D., A method for implementing time-integral constitutive equations in commercial CFD packages , J. Non-Newtonian Fluid Mech., 86, (1999), 337.

[10] A. Goublomme, M.J. Crochet, Numerical prediction of extrudate swell of a high-density polyethylene: further results , J. Non-Newt. Fluid Mech. 47 (1993), 281.

[11] A. Goublomme, B. Drailly and M.J.Crochet, Numerical prediction of extrudate swell of a high-density polyethylene , J. Non-Newt. Fluid Mech., 44 (1992), 171.

[12] H.J. Park, D.G. Kiriakidis, E. Mitsoulis, Birefringence studies in die flows of an HDPE melt, J. Rheol. 36 (1992), 1563.

[13] Olley, P., An adaptation of the separable KBKZ equation for comparable response in planar and axisymmetric flow , J. Non-Newtonian Fluid Mech, 95 (2000), 35.

[14] Mitsoulis, E., Numerical simulation of entry flow of the IUPAC-LDPE melt , J. Non-Newtonian Fluid Mech., 97 (2001), 13.

[15] Mitsoulis, E., Entry flow of LDPE melts in a planar contraction , J. Non-Newtonian Fluid Mech., 111 (2003), 41.

[16] Wagner, M.H. and Schaeffer, J., Nonlinear strain measures for general biaxial extension of polymer melts,J. Rheol., 36 (1992), 1.

[17] Wagner, M.H. and Schaeffer, Assessment of nonlinear strain measures for extensional and shearing flows of polymer melts, J., Rheol. Acta, 33 (1994), 506.

[18] Wagner, M.H., Ehrecke, P., Hachmann, P., Meissner, J., A constitutive analysis of uniaxial, equibiaxial and planar extension of a commercial linear high-density polyethylene melt J.Rheol., 42 (1998), 621.

[19] Wagner, M.H., Bastian, H., Hachmann, P., Meissner, J., Kurzbeck, S., Munstedt, H., Langouche, F., The strain-hardening behaviour of linear and long-chain branched polyolefin melts in extensional flows, Rheol. Acta , 39 (2000), 97.

[20] Wagner, M.H., Rubio, P., Bastian, H., The molecular stress function model for polydisperse polymer melts with dissipative convective constraint release J.Rheol, 45 (2001), 1387.

[21] Marrucci, G., Dynamics of entanglements: A nonlinear model consistent with the Cox-Merz rule , J. Non-Newtonian Fluid Mech., 62 (1996), 279.

[22] Peters, E.A.J.F, Hulsen, M.A., and van den Brule, B.H.A.A., Instationary Eulerian viscoelastic flow simulations using time seperable Rivlin-Sawyers constitutive equations, J. Non-Newtonian Fluid Mech., 89 (2000), 209.

[23] Rasmussen, H.K., Lagrangian viscoelastic flow computations using the Rivlin-Sawyers constitutive model, J. Non-Newtonian Fluid Mech., 92 (2000), 227.

[24] Rasmussen, H.K., Lagrangian viscoelastic flow computations using a generalised molecular stress function model, J. Non-Newtonian Fluid Mech., 106 (2002), 107.

[25] Wapperom, P., and Keunnings, R., Simulation of linear polymer melts in transient complex flow, J. Non-Newtonian Fluid Mech., 95 (2000), 67.

[26] McLeish, T.C.B, Larson, R.G., Molecular constitutive equations for a class of branched polymers: The pom-pom polymer ,J. Rheol. 42 (1998), 81.

[27] Milner, S.T., McLeish, T.C.B, Likhtman, A.E., Microscopic theory of convective constraint release , J.Rheol., 45 (2001), 539.

[28] Arjen, C.B.B, Grillet, A.M., Peters, G.W.M., Baaijens, F.P.T., Viscoelastic analysis of complex polymer melt flows using the eXtended Pom–Pom model , J. Non Newtonian Fluid Mech., 108 (2002), 301.

[29] Wilco, M.H.V., Peters, G.W.M., Baaijens, F.P.T, Numerical simulations of the planar contraction flow for a polyethylene melt using the XPP model , J. Non Newtonian Fluid Mech., 117 (2004), 73.

[30] Ianniruberto, G, Marrucci, G., A simple constitutive equation for entangled polymers with chain stretch , J.Rheol., 45 (2001), 1305.

[31] Ianniruberto, G, Marrucci, G., A multi-mode CCR model for entangled polymers with chain stretch , J. Non Newtonian Fluid Mech., 102 (2002), 385.

[32] Currie, P.K., Calculations on the Doi-Edwards Model for Concentrated Polymer Systems, in "Rheology", the Proc. of the ninth Inter. Congress on Rheology, Acapulco, Mexico (1984)

[33] van Heel, A.G.P, Hulsen, M.A., and van den Brule, B.H.A.A, Simulation of the Doi-Edwards model in complex flow, J. Rheol., 43 (1999), 1239.

[34] Laun, J.M., Description of the non-linear shear behaviour of a low density polyethylene melt by means of an experimentally determined strain dependent memory function, Rheol. Acta., 17 (1978), 1.

[35] Laun, J.M. and Munstedt, H., Elongational behaviour of a low density polyethylene melt, Rheol. Acta., 17 (1978), 415.

[36] Meissner, J., Basic parameters, melt rheology, processing and end use properties of three similar low density polyethylene samples, Pure Appl. Chem., 42 (1975), 553-612

[37] Luo, X.-L., Mitsoulis, E., A numerical study of the effect of elongational viscosity on vortex growth in contraction flows of polyethylene melts, J. Rheol., 34 (1990), 309.

[38] Luo, X.-L. and Tanner, R.I., A streamline element scheme for solving viscoelastic flow problems part II: Integral constitutive models, J. Non Newtonian Fluid Mech., 22 (1986), 61.

[39] Chapra, S.C., and Canale, R.P., Numerical methods for engineers, McGraw-Hill Publishers, third edition (1998), ISBN 0-07-010938-9

[40] M. Viriyayuthakon and B. Caswell, Finite element simulation of viscoelastic flow, J. Non Newtonian Fluid Mech., 6 (1980), 245.

[41] Sun, J., Phan-Thien, N., and Tanner, R.I., An adaptive viscoelastic stress splitting scheme and its applications: AVSS/SI and AVSS/SUPG, J. Non Newtonian Fluid Mech., 65 (1996), 75.
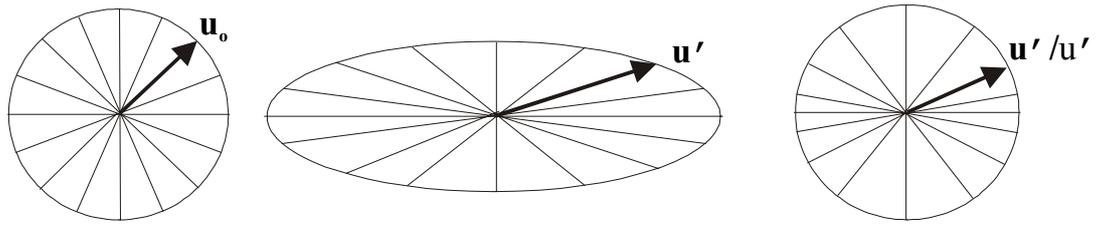
List of figure captions:

Figure 1 Schematic of tube deformations: $\mathbf{u_o}$ is the original undeformed vector, $\mathbf{u'}$ is the deformed vector given by $\mathbf{u'}=\mathbf{F}^{-1}\mathbf{u_o}$, and $\mathbf{u'}\,/\,u'$ is the normalised deformed vector.
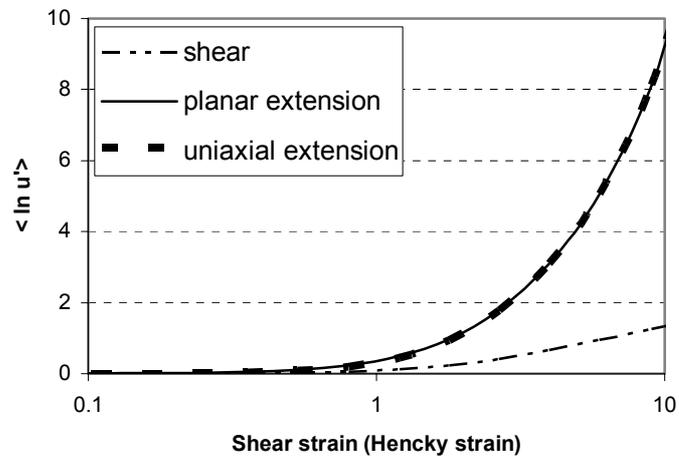
Figure 2 Variation of $<\ln u'>$ with shear or Hencky strain in shear, planar extensional, and uniaxial extensional flows
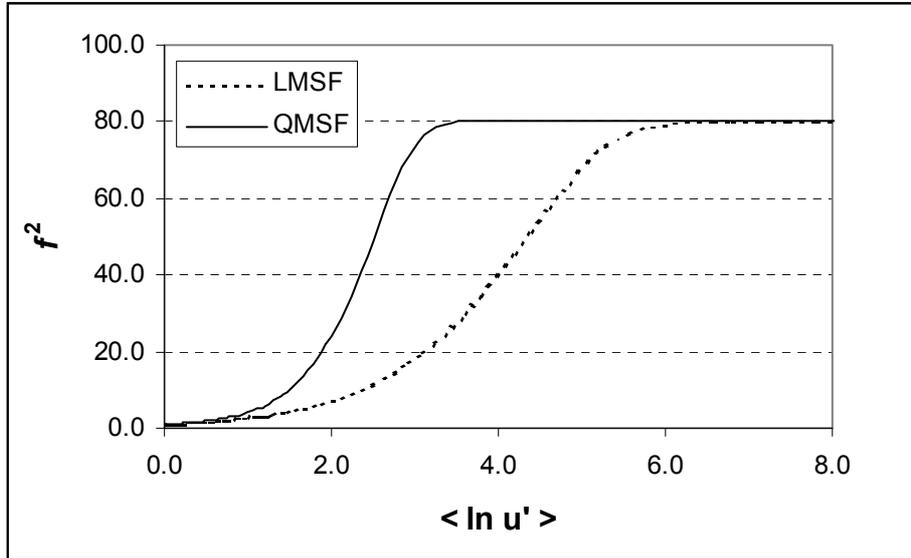
Figure 3 Variation of f^2 with $<\ln u'>$ for the Linear MSF, and Quadratic MSF models. f^2_{max} is set to 80.0 in both cases

Figure 4 Elemental area, $d\Omega$, of the surface of a sphere of radius r

Figure 5 Comparison between QMSF and transient viscosity data for IUPAC LDPE at 125°C

Figure 6 Comparison between experimental data for planar elongational viscosity at $0.05s^{-1}$ for IUPAC LDPE, and the QMSF, LMSF, and adapted KBKZ models

Figure 7 Comparison of QMSF predictions for uniaxial elongational viscosity, shear viscosity, and N1 against experimental results for IUPAC LDPE at 150°C. Prediction for planar elongational viscosity is also shown (dotted). The value for the single parameter f^2_{max} (=80.0) was obtained from transient data.

Figure 8 Comparison of pressure contours in fully developed region of die slit.
(a) time-integral using $(\mathbf{C}^{-1} - \mathbf{I})\,h(I_1, I_2)$, (b) time-integral using Doi-Edwards tensor, (c) time-integral using QMSF tensor (strain hardening)

Figure 9 Vortex details for the QMSF model and for the adapted KBKZ model in planar contraction flow; contours are plotted at integer multiples of 0.1%

Figure 10 Comparison of opening angles obtained for three models in 8:1 planar contraction flow

Figure 11 Comparison of vortex intensity obtained for three models in 8:1 planar contraction flow

Figure 12 Comparison of correction pressures obtained for three models in 8:1 planar contraction flow

Figure 13 Comparison of opening angles obtained for three models in 4:1 axisymmetric contraction flow

Figure 14 Comparison of vortex intensities obtained for three models in 4:1 axisymmetric contraction flow

Figure 15 Comparison of correction pressures obtained for three models in 4:1 axisymmetric contraction flow

Tables:

Table 1 Rheological data for IUPAC LDPE at 125°C, 150°C, and 160°C

i	1	2	3	4	5	6	7	8
g_i (Pa)	1.29×10^5	9.48×10^4	5.86×10^4	2.67×10^4	9.80×10^3	1.89×10^3	1.80×10^2	1.00×10^0
λ_i (s) (150°C)	10.0×10^{-5}	10.0×10^{-4}	10.0×10^{-3}	10.0×10^{-2}	10.0×10^{-1}	10.0×10^0	10.0×10^1	10.0×10^2
λ_i (s) (160°C)	7.01×10^{-5}	7.01×10^{-4}	7.01×10^{-3}	7.01×10^{-2}	7.01×10^{-1}	7.01×10^0	7.01×10^1	7.01×10^2
λ_i (s) (125°C)	26.2×10^{-5}	26.2×10^{-4}	26.2×10^{-3}	26.2×10^{-2}	26.2×10^{-1}	26.2×10^0	26.2×10^1	26.2×10^2

Table 2 Specification of the 'PSM KBKZ and the 'adapted' KBKZ used in this work, and their parameters

Reference name	Specification	Adjustable parameters
'PSM' KBKZ	$\tau(t) = \int_{-\infty}^{t} m(t,t') \mathbf{C}^{-1}(t,t') \dfrac{\alpha}{\alpha + \beta I_1 + (1-\beta)I_2 - 3} \, dt'$	$\alpha = 14.38$ $\beta = 0.018$
'adapted' KBKZ	$\tau(t) = \int_{-\infty}^{t} m(t,t') \mathbf{C}^{-1}(t,t') \dfrac{\alpha}{\alpha + \beta S^2 + (1-\beta)S} \, dt'$, where $S^2 = I_1 - 3$	$\alpha = 2.5$ $\beta = 0.003$

Figure 1 Schematic of tube deformations: $\mathbf{u_o}$ is the original undeformed vector, $\mathbf{u'}$ is the deformed vector given by $\mathbf{u'}=\mathbf{F}^{-1}\mathbf{u_o}$, and $\mathbf{u'}$ / u' is the normalised deformed vector.

Figure 2 Variation of <ln u'> with shear or Hencky strain in shear, planar extensional, and uniaxial extensional flows

Figure 3 Variation of f^2 with <ln u'> for the Linear MSF, and Quadratic MSF models. f^2_{max} is set to 80.0 in both cases

$$d\Omega = r^2 \sin\theta \, d\theta \, d\phi$$

r sinθ dφ

r dθ

θ

φ

Figure 4 Elemental area, dΩ, of the surface of a sphere of radius r

Figure 5 Comparison between QMSF and transient viscosity data for IUPAC LDPE at 125°C

Figure 6 Comparison between experimental data for planar elongational viscosity at 0.05s^{-1} for IUPAC LDPE, and the QMSF, LMSF, and adapted KBKZ models

Figure 7 Comparison of QMSF predictions for uniaxial elongational viscosity, shear viscosity, and N1 against experimental results for IUPAC LDPE at 150°C. Prediction for planar elongational viscosity is also shown (dotted). The value for the single parameter f^2_{max} (=80.0) was obtained from transient data.

Figure 8 Comparison of pressure contours in fully developed region of die slit.
(a) time-integral using $(\mathbf{C^{-1}} - \mathbf{I})$ $h(I_1, I_2)$, (b) time-integral using Doi-Edwards tensor,
(c) time-integral using QMSF tensor (strain hardening)

Adapted KBKZ

Quadratic Molecular Strain Function

$\dot{\gamma}_a = 4s^{-1}$

$\dot{\gamma}_a = 16s^{-1}$

$\dot{\gamma}_a = 64s^{-1}$

Figure 9 Vortex details for the QMSF model and for the adapted KBKZ model in planar contraction flow; contours are plotted at integer multiples of 0.1%

Figure 10 Comparison of opening angles obtained for three models in 8:1 planar contraction flow

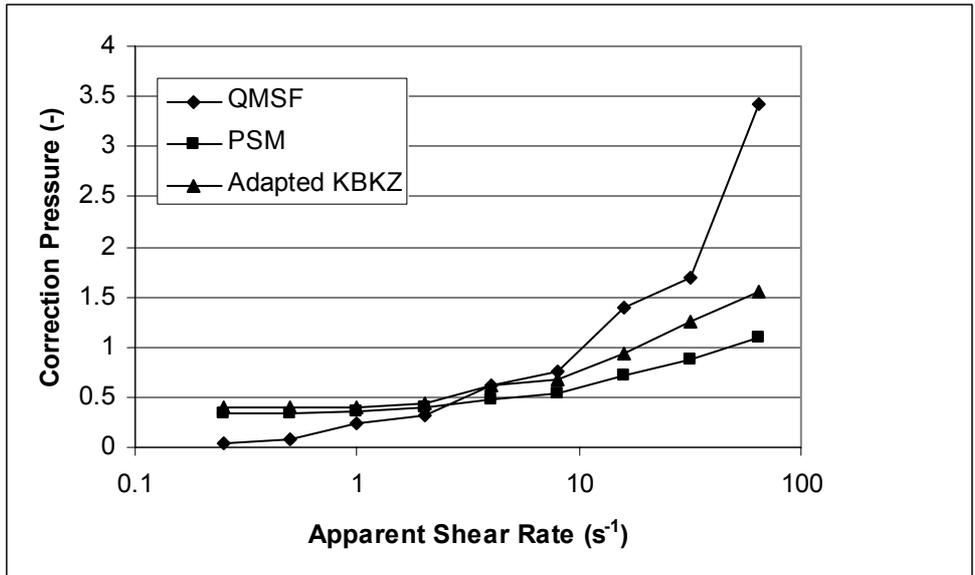Figure 11 Comparison of vortex intensity obtained for three models in 8:1 planar contraction flow

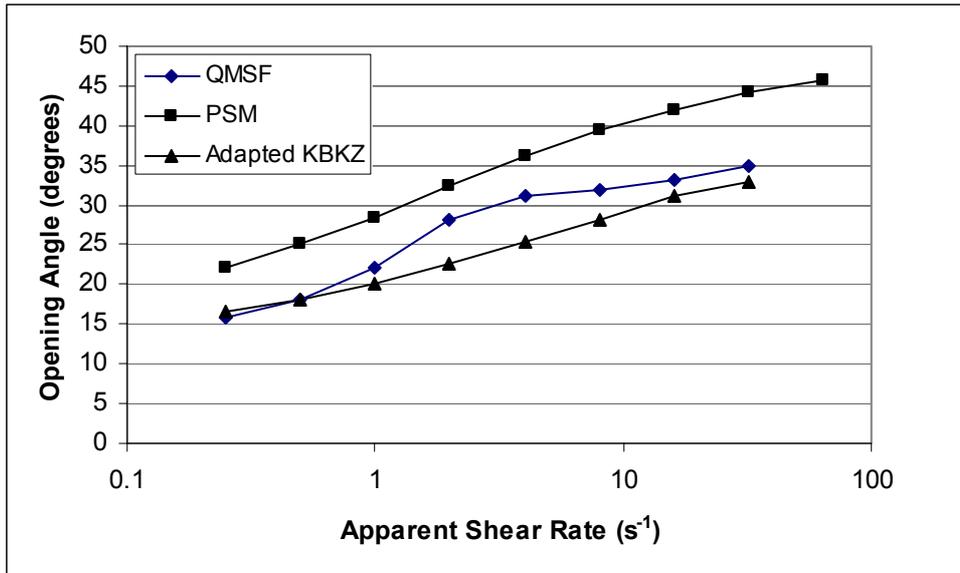Figure 12 Comparison of correction pressures obtained for three models in 8:1 planar contraction flow

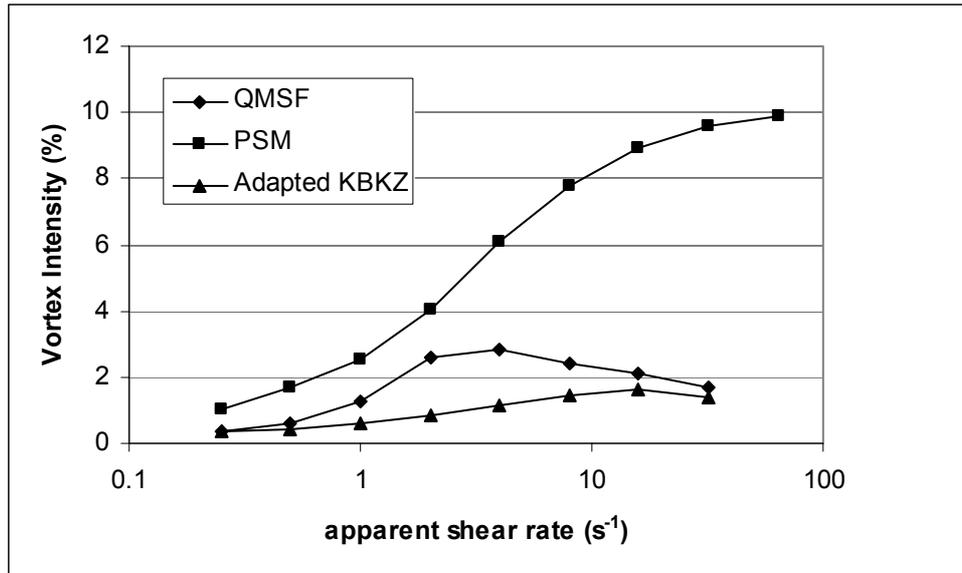Figure 13 Comparison of opening angles obtained for three models in 4:1 axisymmetric contraction flow

Figure 14 Comparison of vortex intensities obtained for three models in 4:1 axisymmetric contraction flow
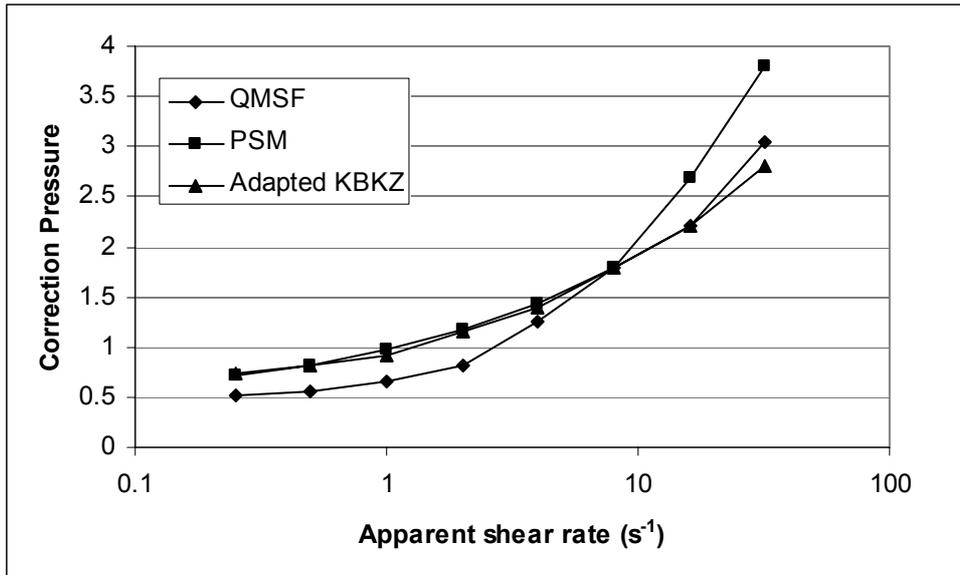
Figure 15 Comparison of correction pressures obtained for three models in 4:1 axisymmetric contraction flow